Microphysical Retrievals from Dual-Polarization Radar Measurements at X Band

EUGENIO GORGUCCI

Istituto di Scienze dell'Atmosfera e del Clima (CNR), Rome, Italy

V. CHANDRASEKAR

Colorado State University, Fort Collins, Colorado

LUCA BALDINI

Istituto di Scienze dell'Atmosfera e del Clima (CNR), Rome, Italy

(Manuscript received 9 January 2007, in final form 24 September 2007)

ABSTRACT

The recent advances in attenuation correction methodology are based on the use of a constraint represented by the total amount of the attenuation encountered along the path shared over each range bin in the path. This technique is improved by using the inner self-consistency of radar measurements. The full self-consistency methodology provides an optimization procedure for obtaining the best estimate of specific and cumulative attenuation and specific and cumulative differential attenuation.

The main goal of the study is to examine drop size distribution (DSD) retrieval from X-band radar measurements after attenuation correction. A new technique for estimating the slope of a linear axis ratio model from polarimetric radar measurements at attenuated frequencies is envisioned. A new set of improved algorithms immune to variability in the raindrop shape–size relation are presented for the estimation of the governing parameters characterizing a gamma raindrop size distribution.

Simulations based on the use of profiles of gamma drop size distribution parameters obtained from S-band observations are used for quantitative analysis. Radar data collected by the NOAA/Earth System Research Laboratory (ESRL) X-band polarimetric radar are used to provide examples of the DSD parameter retrievals using attenuation-corrected radar measurements. Retrievals agree fairly well with disdrometer data. The radar data are also used to observe the prevailing shape of raindrops directly from the radar measurements. A significant result is that oblateness of drops is bounded between the two shape models of Pruppacher and Beard, and Beard and Chuang, the former representing the upper boundary and the latter the lower boundary.

1. Introduction

The distribution of raindrop sizes [drop size distribution (DSD)] as well as shapes is of central importance in determining the electromagnetic scattering properties of rain-filled media. These effects, in turn, are embodied in radar parameters of interest here: the reflectivity factor (Z); differential reflectivity (Z_{dr}), which is the ratio of reflectivities at h and v polarization states ($Z_{h,v}$; Seliga and Bringi 1976); and specific differential phase (K_{dp}), which is due to the propagation phase difference between h and v polarization states (Seliga and Bringi 1978). Many studies of dual-polarization radar have shown that observations at S band can be used to derive raindrop size distribution parameters (Gorgucci et al. 2002a; Bringi et al. 2003; Brandes et al. 2003) and mean raindrop shape (Gorgucci et al. 2000; Moisseev et al. 2006; Gorgucci et al. 2006a).

Because of negligible attenuation, the study of microphysical retrievals from dual-polarization radar has been predominantly restricted to S-band frequencies. However, in Europe, polarimetric C-band radar systems are gaining ground for use in meteorological applications (Gorgucci et al. 2002b; Illingworth and

Corresponding author address: Eugenio Gorgucci, Istituto di Scienze dell'Atmosfera e del Clima (CNR), Area di Ricerca Roma-Tor Vergata Via Fosso del Cavaliere, 100-00133 Rome, Italy.
E-mail: e.gorgucci@isac.cnr.it

DOI: 10.1175/2007JTECHA971.1

Thompson 2005). Furthermore, there has recently been renewed interest in the use of X-band frequencies because of their specific advantages, such as applications to rainfall estimation in light rain (Matrosov et al. 2002) and monitoring of sensitive areas that are inadequately covered by operational networks (Anagnostou et al. 2004), as well as the radar network concept introduced by the Center for Collaborative Adaptive Sensing of the Atmosphere (CASA; Chandrasekar et al. 2004). In the last decade, this extensive use of polarimetric radar systems at higher frequencies has been made easier by advances in correcting attenuation techniques based on the use of polarimetric measurements (Bringi et al. 1990; Testud et al. 2000; Bringi and Chandrasekar 2001). The initial set of attenuation correction algorithms was built from the differential propagation phase (Φ_{dp}).

Among the new algorithms that have been proposed, one of the popular approaches is the algorithm of Testud et al. (2000), which adopts a final value constraint as used in spaceborne radar. The final value constraint was developed for ground-based radar by converting the cumulative differential phase to cumulative attenuation. In fact, from calculations based on the scattering properties of individual drops, the relationship between K_{dp} and the specific attenuation (α_h) has been found to be nearly linear. However, this relationship depends on the temperature as well as drop size and drop shape variability, which are directly translated as an error in the correction procedure. Bringi et al. (2001) proposed a variation that does not assume a priori knowledge of the constant coefficient (a_h) converting K_{dp} into α_h, which, rather, is assumed to lie in a predetermined range. The optimal value of a_h is determined via a minimization process for each radar data beam.

One of the advantages of polarimetric radar measurement is internal self-consistency (Scarchilli et al. 1996). This principle, introduced for the first time by Gorgucci et al. (1992), takes advantage of the synergy between the radar measurements of reflectivity factor, differential reflectivity, and specific differential phase. Recently, it has been applied in a new methodology called the self-consistency (SC) method for attenuation and differential attenuation (α_d) correction at X band (Gorgucci et al. 2006b). The technique, enforcing self-consistency between K_{dp} and corrected Z_h and Z_{dr} measurements, improves attenuation and differential attenuation accuracy provided by the methods using Φ_{dp} as a constraint. In addition, Gorgucci and Baldini (2007) have proposed and tested at C band an optimization of the SC method to make the procedure fully self-consistent (FSC). Their study shows excellent performance with negligible bias and very little normalized standard error compared to other correcting attenuation techniques. This paper takes the next step—the retrieval of DSD parameters using the attenuation-corrected polarimetric radar measurements at X band.

The paper is organized as follows. In section 2, the background of DSD microphysics is briefly discussed. Section 3 describes the basic algorithms used in the paper to retrieve the DSD by means of polarimetric radar measurements, and section 4 introduces the attenuation correction algorithms, showing the evaluation of their performance. In section 5, simulation studies are presented to analyze the performance of DSD retrieval using corrected radar measurements. An example of DSD retrieval from real X-band polarimetric radar data with a comparison with disdrometer data is presented in section 6. Conclusions are summarized in section 7.

2. Rain microphysics

Accurate rain rate estimation requires the characterization of rain microphysics, particularly its two basic components: DSD and effective drop shape (EDS). In fact, microphysical processes of evaporation, accretion, and precipitation rates are all related by DSD, while the physical process of collision, which can cause coalescence and breakup, affects the drop shape, which most likely will depend on collisional energy or momentum.

a. Raindrop size distribution

The measurement of raindrop size distribution over broad areas is important for large-scale rain microphysical properties. Raindrop size distribution changes, with geographical location strongly influencing rainfall characteristics (Bringi et al. 2003). The distribution of drop sizes in rain usually contains a wide range of drop diameters. Small drops generally outnumber large drops, but as the intensity of the rainfall increases, the number of larger drops grows. This evolution of raindrop size distribution is determined by coalescence, collisional breakup, and evaporation. Accurate characterization of raindrop size distribution and the estimation of DSD parameters using remote measurements are useful for improving the accuracy of rainfall intensity observed by weather radar and satellite observations. In this context, polarimetric radar measurements have been used to reach the long-standing goal of raindrop size distribution estimation over large spatial and temporal scales (Gorgucci et al. 2002a; Bringi et al. 2003).

Raindrop size distribution describes the probability density distribution function of raindrop sizes. In prac-

tice, the normalized histogram of raindrop sizes (normalized with respect to the total number of observed raindrops) converges to the probability density function of raindrop sizes. A gamma distribution model has been shown to adequately describe many of the natural variations in the shape of the raindrop size distribution (Ulbrich 1983). The gamma raindrop size distribution can be expressed as

$$N(D) = n_c f_D(D)\ (\mathrm{m}^{-3}\ \mathrm{mm}^{-1}), \tag{1}$$

where $N(D)$ is the number of raindrops per unit volume per unit size interval (D to $D + \Delta D$), n_c is the number concentration, and $f_D(D)$ is the probability density function (pdf). When $f_D(D)$ is of the gamma form it is given by

$$f_D(D) = \frac{\Lambda^{\mu+1}}{\Gamma(\mu+1)} e^{-\Lambda D} D^{\mu}, \quad \mu > -1, \tag{2}$$

and any other gamma form, such as the one introduced by Ulbrich (1983),

$$N(D) = N_0 D^{\mu} e^{-\Lambda D}, \tag{3}$$

can be derived from this fundamental notion of raindrop size distribution. The parameters N_0 (the intercept), Λ (the slope), and μ (the shape) characterize the gamma pdf. It must be noted that any function used to describe $N(D)$ when integrated over D must yield the total number concentration to qualify as a DSD function. This property is a direct consequence of the fundamental result that any probability density function must integrate to unity. The relation between D_0, μ, and Λ is given by

$$\Lambda D_0 \cong 3.67 + \mu, \tag{4}$$

where D_0 is the drop median diameter defined as

$$\int_0^{D_0} D^3 N(D)\, dD = \int_{D_0}^{\infty} D^3 N(D)\, dD. \tag{5}$$

Using (4), $f_D(D)$, the gamma pdf described by (2), can be written in terms of D_0 and μ as

$$f_D(D) = \frac{(3.67+\mu)^{\mu+1}}{\Gamma(\mu+1) D_0} \left(\frac{D}{D_0}\right)^{\mu} \exp\left[-(3.67+\mu)\frac{D}{D_0}\right]. \tag{6}$$

To compare the probability density function of D in the presence of varying water contents, the concept of scaling the DSD has been used by several authors (Testud et al. 2000; Illingworth and Blackman 2002).

The corresponding form of $N(D)$ can be expressed as

$$N(D) = N_w f(\mu) \left(\frac{D}{D_0}\right)^{\mu} \exp\left[-(3.67+\mu)\frac{D}{D_0}\right], \tag{7}$$

where N_w is the scaled version of N_0 defined in (3):

$$N_w = \frac{N_0}{f(\mu)} D_0^{\mu} \tag{8a}$$

and

$$f(\mu) = \frac{6}{(3.67)^4}\left[\frac{(3.67+\mu)^{\mu+4}}{\Gamma(\mu+4)}\right], \tag{8b}$$

with $f(0) = 1$ and $f(\mu)$ is a unitless function of μ. One interpretation of N_w is that it is the intercept of an equivalent exponential distribution with the same water content and D_0 as the gamma DSD (Bringi and Chandrasekar 2001). Thus N_w, D_0, and μ form the three parameters of the gamma DSD.

b. Effective drop shape

Wind tunnel measurements and the 2D video disdrometer as well as in situ observations using airborne 2D probes indicate that the shape of raindrops can be approximated by oblate spheroids described by semimajor axis a and semiminor axis b. The axis ratio of the raindrop (r) is given by

$$r = \frac{b}{a}. \tag{9}$$

The shape–size relation can be approximated by a straight line (Gorgucci et al. 2000) given by

$$r(D) = 1.03 - \beta D. \tag{10}$$

In (10), $r = 1$ when $D \le 0.03/\beta$, where β is the magnitude of the slope of the shape–size relationship given by

$$\beta = -\frac{dr}{dD}\ (\mathrm{mm}^{-1}). \tag{11}$$

The linear fit to the wind tunnel data of Pruppacher and Beard (1970) corresponds to $\beta = 0.062\ \mathrm{mm}^{-1}$ (the resulting drop shape model will be hereafter referred as PB). In general, given a DSD it is possible to define a mass-weighted mean axis ratio as

$$\bar{r}_m = \frac{\int_0^{\infty} D^3 N(D) r(D)\, dD}{\int_0^{\infty} D^3 N(D)\, dD}. \tag{12}$$

In this way (10), taking (12) into account, can be used to define for the given DSD an effective drop shape expressed as

$$\beta_e = \frac{1.03 - \bar{r}_m}{\overline{D}_m}, \tag{13}$$

where $\overline{D}_m$ is the mass-weighted mean drop diameter. Equation (13) allows the definition of an equivalent

linear relation in the case that (9) is not linear. In fact, if the mean axis ratio versus D relation is nonlinear, it is always possible to define a linear relation that results in the same $K_{\rm dp}$ (Bringi et al. 2003).

3. Polarimetric radar retrieval of EDS and DSD

Seliga et al. (1981) showed that for an exponential distribution, the two parameters of the DSD, N_0 and D_0, can be estimated using $Z_{\rm dr}$ and Z_h. Using an equilibrium raindrop shape model, they employed a two-step procedure where first they estimated D_0 from $Z_{\rm dr}$ and subsequently used this value jointly to Z_h to estimate N_0. This procedure can essentially also be applied for a normalized gamma DSD and the generic drop shape model described by (10).

Gorgucci et al. (2006a) showed that by collapsing the self-consistency principle onto a two-dimensional space defined by the two variables $K_{\rm dp}/Z_h$ and $Z_{\rm dr}$, the influence of DSD is minimized so that the drop shape variation can be observed. At S band, they used this approach to get information on the prevailing shape of the raindrop along the path directly from polarimetric radar measurements. Using this methodology, it was found that the different contours of drop shape frequencies are centered on a line that corresponds to slightly more spherical shapes than those described by the PB model, but showing a similar linear relation. This result suggests that replacing the β algorithm proposed in Gorgucci et al. (2000) with a function of the two variables $K_{\rm dp}/Z_h$ and $Z_{\rm dr}$ gives results that are more robust with regard to DSD variations. The new algorithm takes the form of

$$\beta_e = c_1\left(\frac{K_{\rm dp}}{Z_h}\right)^{a_1}\xi_{\rm dr}^{b_1}\,({\rm mm}^{-1}). \tag{14}$$

A simulation was performed for the same conditions mentioned above to find the parameters a, b, and c. Once the gamma DSD is given in the form of (7), it is possible to compute radar parameters such as Z_h, $Z_{\rm dr}$, and $K_{\rm dp}$ for the various β of the drop shape defined by (10). Under these conditions and at a temperature of 20°, radar parameters are computed for widely varying DSDs by randomly choosing N_w, D_0, μ, and β over the following ranges:

$$\begin{aligned} 3 &\le \log_{10} N_w \le 5\ ({\rm m}^{-3}\,{\rm mm}^{-1})\\ 0.5 &< D_0 < 3.5\ ({\rm mm})\\ -1 &< \mu \le 5\\ 0.04 &< \beta < 0.08\ ({\rm mm}^{-1}), \end{aligned} \tag{15}$$

with the further constraints of $(10\log_{10} Z_h) < 55$ dB and $R < 300$ mm h^{-1}. The range variability (15) falls within the range of parameters suggested by Ulbrich (1983). Once Z_h, $Z_{\rm dr}$, and $K_{\rm dp}$ measurements are simulated, a nonlinear regression analysis is performed to estimate the coefficients in (14). In Table 1, the values of the coefficients are reported for S, C, and X band (3, 5.4, and 9.3 GHz, respectively). At X band, (14) is characterized by a correlation coefficient of 0.974, a normalized standard error (NSE) of 4.3%, and a normalized bias (NB) of 0.15%. NSE is the root-mean-square error normalized with respect to the mean true value, whereas NB is the difference between the mean estimated and true values normalized to the mean true value.

TABLE 1. Coefficient values of the β parameterization (14) for the three basic weather radar bands.

Band	c_1	a_1	b_1
S (3 GHz)	1.220	0.342	1.155
C (5.4 GHz)	1.156	0.367	0.848
X (9.3 GHz)	0.632	0.276	1.212

Gorgucci et al. (2002a) have shown that gamma DSD parameters can be estimated through relationships whose coefficients depend on β. Therefore, once β is estimated from (14), it can be shown that a parameterization for D_0 and N_w can be pursued in the form

$$D_0 = c_2\left(\frac{\xi_{\rm dr} - 0.8}{\beta}\right)^{a_2}({\rm mm}), \tag{16a}$$

$$\log_{10} N_w = c_3\left(\frac{\xi_{\rm dr} - 0.8}{\beta}\right)^{a_3} Z_h^{b_3}, \tag{16b}$$

where N_w is given in mm^{-1} m^{-3}, $\xi_{\rm dr} = 10^{0.1Z_{\rm dr}}$ is the differential reflectivity in linear scale, and Z_h is the reflectivity factor at horizontal polarization (mm^6 m^{-3}). It should be noted here that an equivalent "beta" is being estimated only for algorithmic purposes and not to suggest that the drop shape–size relation in linear. Coefficients of (16a) and (16b) are estimated through the simulation above described and listed in Tables 2 and 3, respectively. A simulation has also been utilized to evaluate the performance of (16). Figure 1a shows the scatterplot of D_0 estimates using (16a) versus true D_0, for widely varying DSD parameters. It can be seen from Fig. 1a that D_0 is estimated fairly well with negligible bias except for $D_0 < 1$ mm. Quantitative analysis of the scatter gives a correlation coefficient of 0.956, an NSE of 12%, and an NB of 0.6%. Figure 1b shows the scatterplot of $\log_{10} N_w$ estimates using (16b) versus the true values for widely varying DSD parameters. Both Figs. 1a and 1b refer to 2000 DSDs. The performance of (16b) is characterized by the following quantitative parameters: correlation coefficient of 0.853, NSE of 7%, and NB of −0.3%.

TABLE 2. Coefficient values of the D_0 parameterization (16a) for the three basic weather radar bands.

Band	c_2	a_2
S (3 GHz)	0.172	1.019
C (5.4 GHz)	0.358	0.662
X (9.3 GHz)	0.202	0.884

4. Attenuation correction of X-band radar measurements

Combining the advantages of both the differential phase–based attenuation correction technique and the rain-profiling algorithm used in spaceborne radar applications, the methodology of Testud et al. [2000; hereafter named differential phase constraint (DPC)] produced an important improvement in the performance of the attenuation correction. The final value constraint was developed by converting the cumulative differential phase to total cumulative attenuation.

At X band, Gorgucci et al. (2006b) proposed a new method for attenuation correction of reflectivity and differential reflectivity based on SC, which constrains each pair of Z_h and Z_{dr} to the corresponding Φ_{dp} along the entire path. Using the values offered by the rain-profiling algorithm (DPC) as an initial guess for the attenuation correction procedure, the self-consistency is then forced with the corrected measurements of Z_h, Z_{dr} in combination with the differential propagation phase for further improving the attenuation correction. An iterative process based on the minimization between reconstructed and measured Φ_{dp} allows for improved attenuation and differential attenuation accuracy compared to the methods that use only Φ_{dp} as a constraint. An independent methodology for optimizing both attenuation and differential attenuation estimation is used.

Starting from the SC method for attenuation and differential attenuation, Gorgucci and Baldini (2007) have proposed, for the C band, an optimization method to make the procedure fully self-consistent. In other words, the quantities Z_h, Z_{dr}, Φ_{dp}, α_h, and α_d are constrained jointly by the self-consistency. The study showed excellent performance, with very little normalized bias and normalized standard error compared to all other correcting attenuation techniques.

TABLE 3. Coefficient values of the $\log_{10} N_w$ parameterization (16b) for the three basic weather radar bands.

Band	c_3	a_3	b_3
S (3 GHz)	8.168	−0.654	0.079
C (5.4 GHz)	6.188	−0.459	0.065
X (9.3 GHz)	7.241	−0.581	0.083

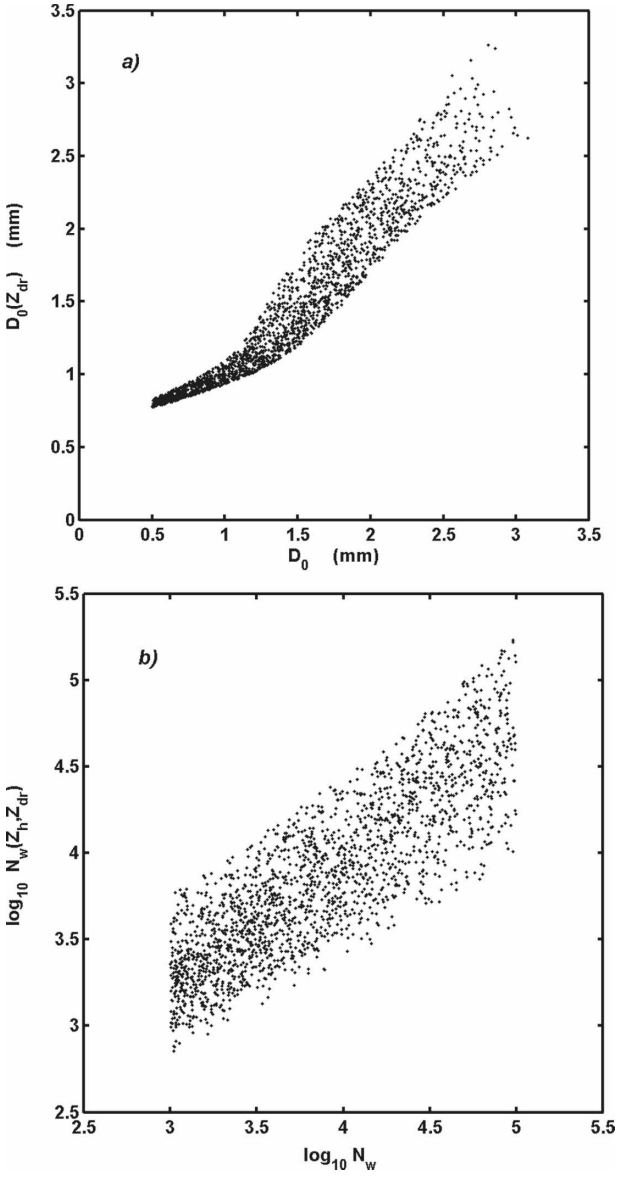

FIG. 1. Scatterplots of (a) D_0 obtained by (16a) and (b) $\log_{10} N_w$ obtained by (16b) vs the corresponding true values for widely varying DSD parameters in (15). The points refer to 2000 DSDs.

Figure 2a shows the normalized bias (black lines) and normalized standard error (gray lines) of specific attenuation estimates using the DPC (dashed line) and FSC (solid line) algorithms as a function of a 15-km rain path with droplets following the PB model. It should be noted that the parameterizations of attenuation and differential attenuation based on the triplet Z_h, Z_{dr}, and K_{dp} used in the FSC methods are built based on the same DSD dataset described above and assuming β to vary between 0.04 and 0.08 mm^{-1}. In this way, the parameterizations will be optimized for varying drop shapes. The profiles refer to the Texas Florida Under-

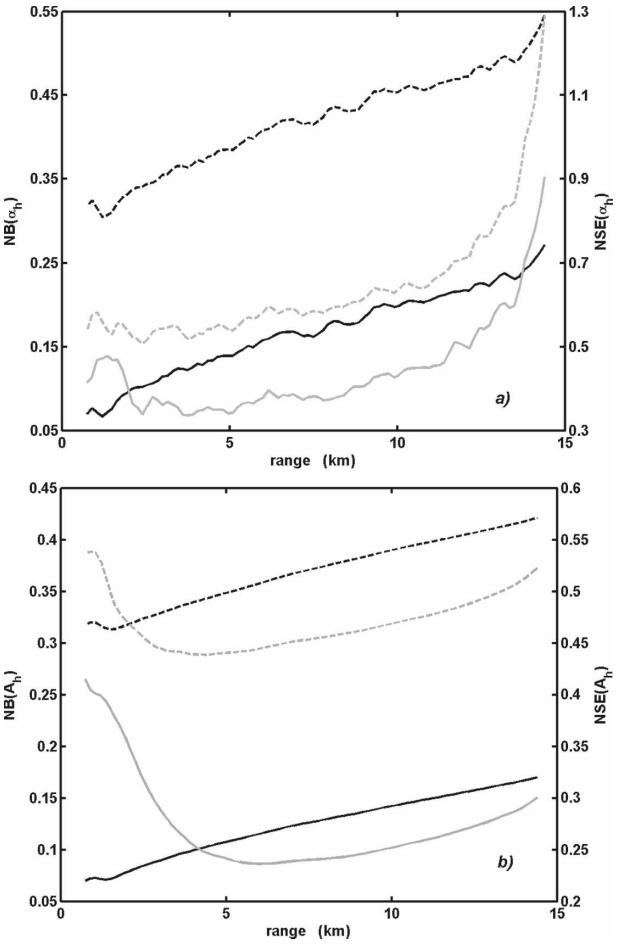

FIG. 2. NB (black lines) and NSE (gray lines) of (a) specific attenuation estimates α_h (DPC; dashed line) and α_h (FSC; solid line) and (b) cumulative attenuation A_h (DPC; dashed line) and A_h (FSC; solid line) as a function of the range. Attenuations of the X-band range profiles, generated from S-band observations, are given by the presence of a 15-km rain path with droplets following the PB model. Error measurements and differential phase upon scattering are included.

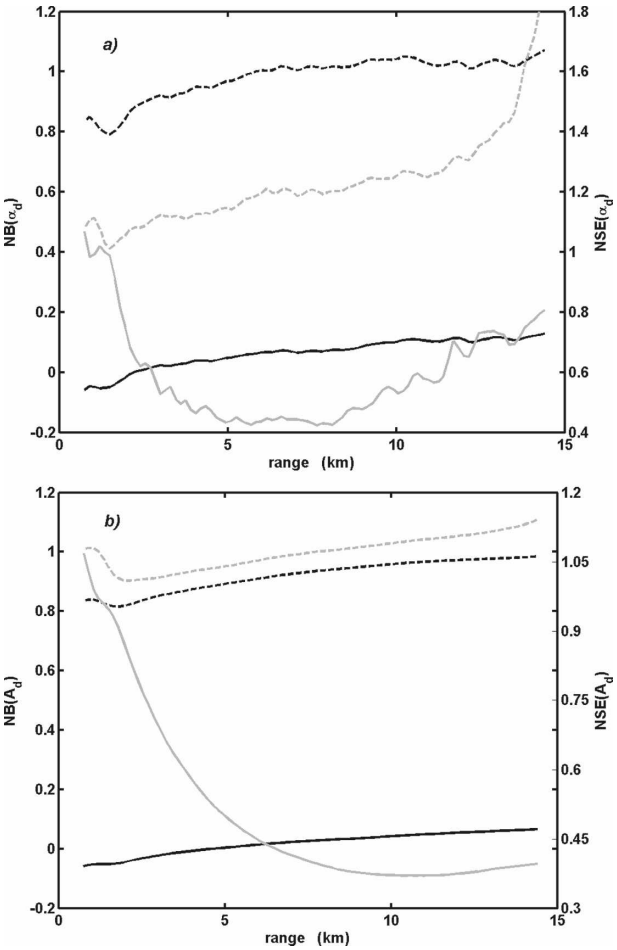

FIG. 3. NB (black lines) and NSE (gray lines) of (a) differential attenuation estimates α_d (DPC; dashed line) and α_d (FSC; solid line) and (b) cumulative differential attenuation A_d (DPC; dashed line) and A_d (FSC; solid line) as a function of the range. Attenuations of the X-band range profiles, generated from S-band observations, are given by the presence of a 15-km rain path with droplets following the PB model. Error measurements and differential phase upon scattering are included.

flight Experiment (TEFLUN-B) campaign described in section 5. Figure 2a illustrates the very good performance of α_h estimations with FSC compared with those obtained by DPC, being characterized by a smaller NB and NSE of about 20%. Figure 2b refers to the same parameters for cumulative attenuation estimates (A_h). In this case, the excellent performance of FSC with respect to DPC is also pointed out by a smaller NB and NSE. In particular, the FSC procedure is suited to removing any systematic bias generated by DSD and drop shape variability along the path.

Figures 3a and 3b show the comparison between differential attenuation and cumulative differential attenuation (A_d) estimated with the FSC in comparison with the DPC algorithm. Except in the first 3 km, where the mean values are much too small, cumulative differential attenuation obtained using FSC presents, on average, an FSE smaller than 50% with respect to the corresponding DPC values; this represents an excellent result.

5. Simulation and analysis

All the most recent techniques designed to correct attenuation and differential attenuation are based on the use of constraints at the end of a fixed path (such as DPC) or distributed along the entire path (such as FSC). In this way, the correction in each bin will depend on an average factor determined by the Φ_{dp} value

relative to the considered bin. The error of this correction can be interpreted as noise that adds to the DSD parameters of the specific bin. To evaluate the effect this has on the DSD retrieved from corrected radar measurements, it would be necessary to know the microphysics in each bin, which is not realistic. The only way to do such an analysis is by simulation. For this purpose, the performance of the DSD retrieval algorithms (16a) and (16b) are evaluated using X-band (9.3 GHz) range profiles generated from S-band (3 GHz) observations. The test data are composed of 6400 profiles that have at least 3° of increase in Φ_{dp}. The simulation methodology is described in Chandrasekar et al. (2006). The S-band radar data used in the analysis were collected by the National Center for Atmospheric Research (NCAR) S-band dual-polarization (S-Pol) Doppler radar during TEFLUN-B. The test data were obtained over rain profiles of 15 km in length containing 100 range bins at a resolution of 0.150 km.

To take account of the different error structures caused by the different radar measurements, the signal fluctuation and the differential phase on backscattering (δ) are also included. Random signal fluctuation is generated (Chandrasekar and Bringi 1987) in such a way that Z_h, Z_{dr}, and Φ_{dp} measurement errors correspond to 1 dB, 0.3 dB, and 3°, respectively.

The method used to study the performance of DSD retrieval is the following:

1) For each real S-band rain profile and for the PB drop shape model, using the self-consistency principle, every range bin is assigned a DSD that generates radar measurements equal to the corresponding real profile values.
2) DSD profiles are used to simulate the radar measurement profiles at X band.
3) Signal random fluctuation is added to the radar measurement profiles.
4) Differential phase on backscattering is added to the path differential phase.
5) For each rain profile, cumulative attenuation and differential attenuation are computed in every range bin, taking the existing DSD into account.
6) The attenuated Z_h and Z_{dr} profiles are obtained by subtracting attenuation and differential attenuation from the corresponding unattenuated values.
7) The FSC correction method is used to estimate attenuation and differential attenuation to obtain corrected Z_h and Z_{dr} profiles.
8) For each path, the estimation of β is obtained by (14) considering Z_h as the mean power along the path, ξ_{dr} the ratio between the mean power at h and v polarization, and K_{dp} the mean value obtained from the finite difference between the end and the beginning of the differential propagation phase profile.
9) In each range bin, D_0 and N_w are computed using (16) and compared to the true value.

TABLE 4. Merit factors of β_e estimation using true, measured, and FSC-corrected values of Z_h and Z_{dr}. Radar measurements, affected by signal fluctuation and differential phase on backscattering, refer to the 15-km path, and K_{dp} is obtained from a finite-difference of the propagation phase profile.

β_e	NB	NSE
True	3.4%	5.1%
Measured	5.3%	7.7%
Corrected	3.6%	6.5%

The performances of the microphysical algorithms (16) are studied using 15-km rain paths with droplets following the PB model. To analyze the different errors, the Eqs. (16) are coded up. The behavior of each parameterization is characterized in terms of NSE and NB.

First, the estimation of β_e is analyzed. To study the performance of (14), following the method described in step 8, β_e has been computed using true, measured, and FSC-corrected values of Z_h and Z_{dr}. Table 4 shows the NB and the NSE of β_e estimation for the three different kinds of profiles. NB and NSE named "true" represent the accuracy of (14) to the DSD variability, whereas NB and NSE named "measured" obtained using profiles affected by measurement errors, attenuation, differential attenuation, and differential phase shift on backscattering characterize the performance of (14) when X-band measurements without any attenuation correction are used. In this case, because of a compensation action between attenuation and differential attenuation (Gorgucci et al. 2006c), β_e results are not much affected by attenuation. The last case, labeled "corrected," refers to the use of FSC-corrected profiles and shows that the FSC technique performs a correction on radar measurements that reduces NB to a value comparable to that obtainable with the true measurements, whereas NSE improves from 7.7% to 6.5%.

Figures 4a and 4b show the NB and the NSE of D_0 estimates using (16a) with true (dashed line), attenuated (dotted line), and corrected values (solid line) of Z_{dr} and β_e as a function of range. The good performance of D_0 estimation is indicated by the very small difference between the values obtained using true and corrected values of Z_{dr} in (16a), about 1% and 2% for NB and NSE, respectively. Of course, this result is primarily due to the goodness of the attenuation correc-

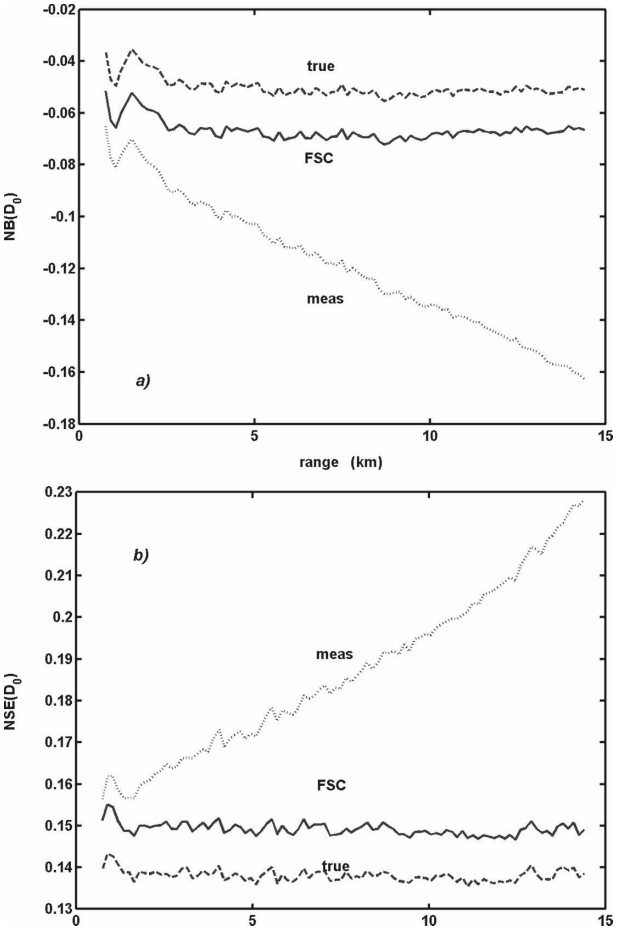

FIG. 4. (a) NB and (b) NSE of D_0 estimates using (16a) computed with true (dashed line), measured (dotted line), and FSC-corrected value (solid line) of Z_{dr} as a function of range.

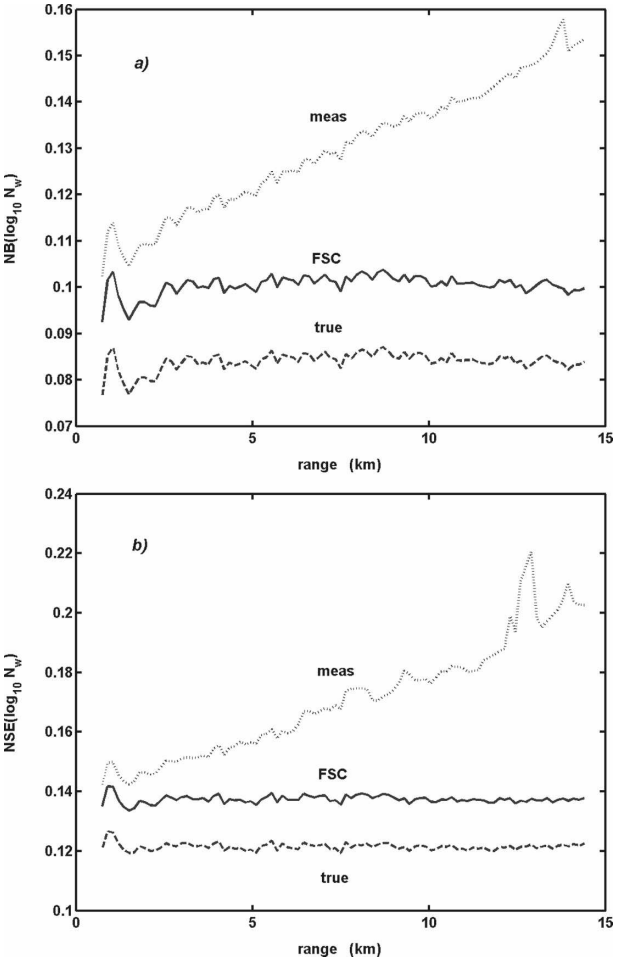

FIG. 5. (a) NB and (b) NSE of $\log_{10} N_w$ estimates using (16b) computed with true (dashed line), measured (dotted line), and FSC-corrected values (solid line) of Z_h and Z_{dr} as a function of range.

tion procedure. In fact, the differences between the true and FSC lines are only due to the attenuation correction procedure, whereas the NB and NSE of the true line give weight to the accuracy of the parameterization. Moreover, it has to be pointed out that increasing NB and NSE with the range obtained using attenuated values is totally removed by the FSC correction technique.

Figures 5a and 5b show the normalized bias and normalized standard error of $\log_{10} N_w$ estimates using (16b) with true (dashed line), attenuated (dotted line), and corrected values (solid line) of Z_h, Z_{dr}, and β_e as a function of range. In this case, the very good performance of (16b) estimations is also highlighted by the small difference, both in NB and NSE, between the values obtained using true and reconstructed values of Z_h, Z_{dr}, and β_e.

Gorgucci et al. (2006a), using radar data collected by the SPol in Florida in 1999, showed that the drop shape retrieved from polarimetric radar data presents a variability that lies between the PB model and the equilibrium model of Beard and Chuang (1987; referred to as BC). For this reason, the algorithms (16a) and (16b) have been analyzed in the presence of a rain medium where raindrops follow the BC model. In this way, it is possible to check the performance of β_e to represent a nonlinear drop shape model as the BC model. The results are shown in Figs. 6 and 7, where NB and NSE of D_0 and $\log_{10} N_w$ estimates are plotted as a function of the range. From a general viewpoint, the metrics show performances similar to those found using the PB drop shape model. The effect related to the use of an equivalent linear relation for the drop shape can be seen by analyzing the true lines. In particular, the estimation of D_0 presents a variation of about 2% and 1% in the NB and NSE, respectively. In the estimation of $\log_{10} N_w$,

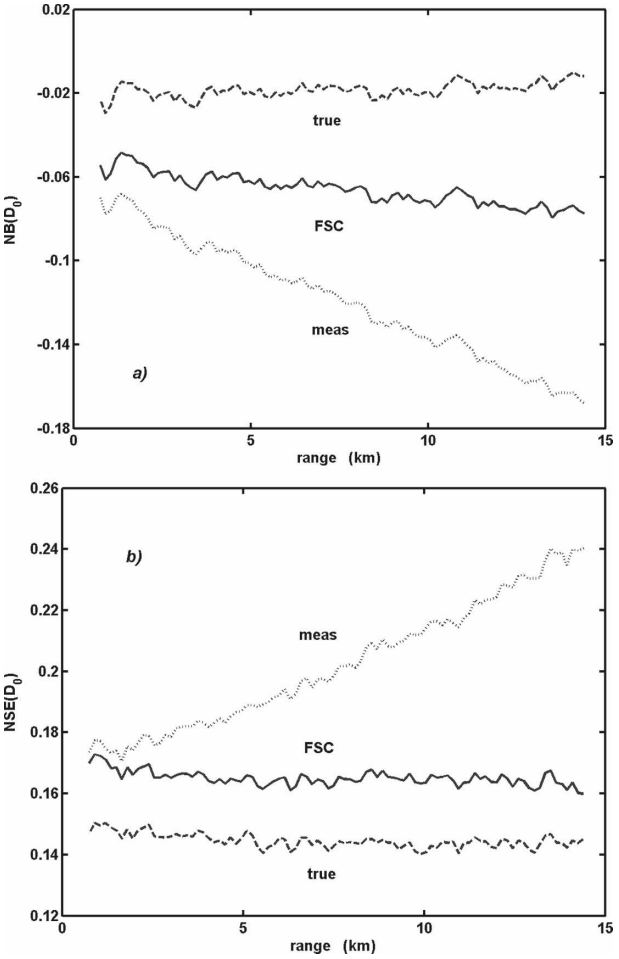

FIG. 6. (a) NB and (b) NSE of D_0 estimates using (16a) computed with true (dashed line), measured (dotted line), and FSC-corrected value (solid line) of $Z_{\rm dr}$ and β_e as a function of range. The raindrops along the path follow the BC drop shape model.

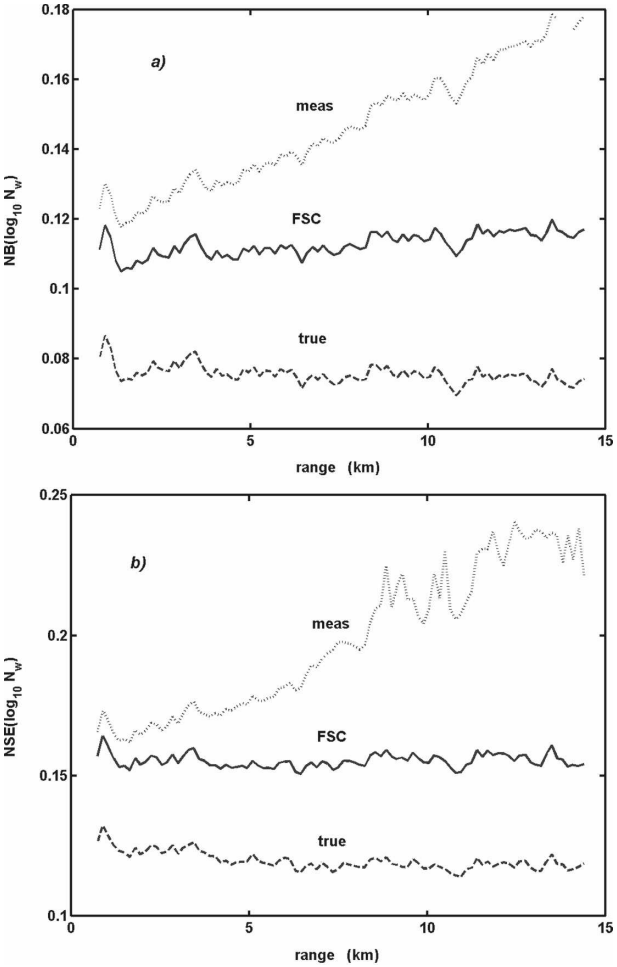

FIG. 7. (a) NB and (b) NSE of $\log_{10} N_w$ estimates using (16b) computed with true (dashed line), measured (dotted line), and FSC-corrected values (solid line) of Z_h, $Z_{\rm dr}$, and β_e as a function of range. The raindrops along the path follow the BC drop shape model.

both NB and NSE present small variations with respect to the PB model. Regarding the robustness of attenuation correction procedure with respect to the drop shape model change, its good performance is pointed out by the small variations of the FSC lines. In conclusion, although NB and NSE obtained from profiles generated using the BC model show higher values than the corresponding values obtained assuming the linear PB model, they still remain well within acceptable limits.

6. Experimental results

The reliability of the microphysical retrieval after attenuation correction has been examined by simulation using reconstructed profiles from real S-band measurements. In this section, we use polarimetric radar data collected by the National Oceanic and Atmospheric Administration/Earth System Research Laboratory (NOAA/ESRL) X-band transportable polarimetric radar (Martner et al. 2001) during the field campaign conducted by Dr. Kummerow at the National Aeronautics and Space Administration (NASA) Wallops Island facility in Virginia. The polarimetric radar measurements were collected using a scheme based on simultaneous transmission and reception at horizontal and vertical polarization states (Matrosov et al. 2002). The data refer to a rain event that took place on 11 April 2001 between 1515 and 1700 UTC. The polarimetric radar measurements were estimated by integrating 256 pulses. To establish the performance of the data collection, a moving window was used to compute the standard deviations of $Z_{\rm dr}$ and $\Phi_{\rm dp}$ that presented modal

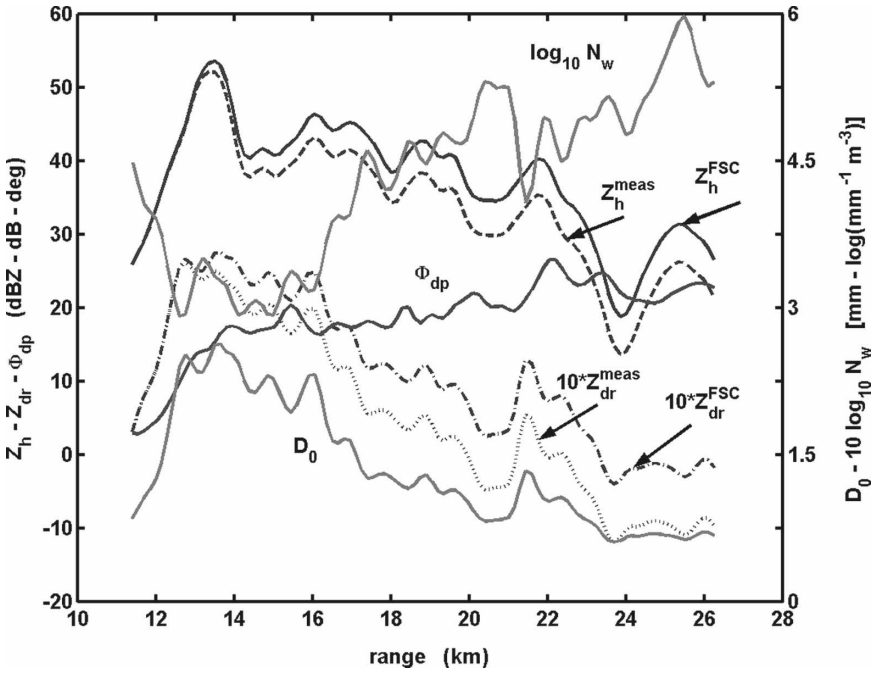

FIG. 8. Example of typical range profile of measured reflectivity, differential reflectivity, and differential propagation phase at the X band. For comparison, corrected Z_h and Z_{dr} profiles using the FSC method are shown. The retrieved profiles of D_0 and $\log_{10} N_w$ are also given. The profile was collected on 11 Apr 2001 at an elevation of 2.7°.

values of 0.065 dB and 0.85°, respectively. These values result in good agreement with the corresponding theoretical computation.

An analysis of the radar images of reflectivity showed, at the beginning of the rainstorm, radar echoes composed of convective rain embedded in stratiform precipitation. The rainstorm changed over time toward a more pronounced stratiform regime.

The test data were obtained from range profiles where the reflectivity factor is greater than 0 dBZ, with the corresponding power at the antenna greater than −110 dBm over at least 15-km consecutive bins. A profile was chosen if it presented more than 3° of increase in Φ_{dp}. Under these conditions, a dataset of about 8500 profiles was selected. The radar data consisted of Z_h, Z_{dr}, and Φ_{dp}, which are available every 150 m in range. The Φ_{dp} was filtered in range using the iterative method of Hubbert and Bringi (1995) in order to minimize the effects due to the phase shift on backscattering. The FSC correction method was performed to estimate attenuation and differential attenuation. These attenuations were used to correct the radar power measurements to obtain corrected Z_h and Z_{dr}.

Figure 8 shows a typical range profile of measured reflectivity, differential reflectivity, and differential propagation phase at the X band with the corrected profiles for Z_h and Z_{dr} using the FSC method. For reference, in the same figure, the retrieved profiles of D_0 and $\log_{10} N_w$ using the retrieval procedure are also shown. The profile exhibits DSD variability with the usual general trend that $\log_{10} N_w$ increases as D_0 decreases.

To retrieve the DSD parameters, the parameter β must be estimated first. The averaged values Z_h, Z_{dr}, and K_{dp} are used to obtain K_{dp}/Z_h and Z_{dr} pairs for each path. Figure 9 shows the distribution of the K_{dp}/Z_h and Z_{dr} values. In the figure as a reference, the behavior of the different averaged K_{dp}/Z_h path values as a function of Z_{dr} for different drop shape models is also plotted. In particular, the linear models characterized by β equal 0.04, 0.05, 0.062, and 0.07 mm^{-1} (referred as β4, β4, PB, and β7, respectively), and the nonlinear models by Beard and Chuang (1987), Andsager et al. (1999), Keenan et al. (2001), and Brandes et al. (2002) (referred as BC, ABL, KZCM, BZV, respectively) are considered. Comparing the distribution of the K_{dp}/Z_h and Z_{dr} values with the corresponding values of the chosen models, a larger amount of information about the prevailing underlying EDS can be obtained. It is important to note that, even if the original drop axis ratio is a nonlinear function, it is possible to define an equivalent linear model that results in the same K_{dp}/Z_h and Z_{dr} pair.

From a general viewpoint, the points of Fig. 9 are

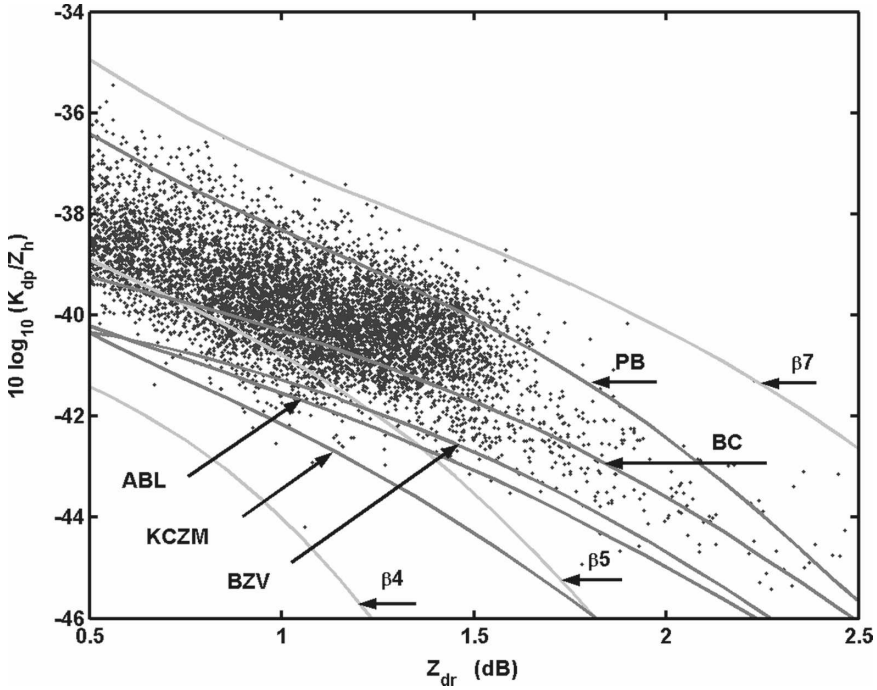

FIG. 9. Scatterplot between the ratio K_{dp}/Z_h as a function of Z_{dr} for X-Pol data collected on 11 Apr 2001 during the campaign conducted at the NASA Wallops Island facility in Virginia. For comparison, averaged values for widely varying DSD obtained from the nonlinear relations of BC, ABL, KCZM, and BZV (dark gray lines), and the linear relations of PB, $\beta = 0.04$ mm^{-1}, $\beta = 0.05$ mm^{-1}, and $\beta = 0.07$ mm^{-1} (light gray lines) are also shown.

located essentially between the PB and BC lines. However, for $Z_{dr} < 1.2$ dB, the line $\beta 5$ appears more suitable to bound the lower part of the scatter. In particular, the mean values of the ratio K_{dp}/Z_h as a function of Z_{dr} present values closer to the BC line and tend to approach the PB line with the increase of Z_{dr}. In other words, raindrops become more oblate as Z_{dr}. increases. Another aspect that needs to be highlighted is that the droplets of the considered precipitation event present on average a drop shape that is more oblate than those described by the BZV, ABL, and KCZM models.

Once β is determined, it is used in the algorithms (16a) and (16b) to retrieve D_0 and N_w. Figure 10 shows the scatter between the values of $\log_{10} N_w$ versus D_0 for the entire dataset collected on 11 April 2001. The values refer to about 840 000 values. The curve presents a clear trend with an inverse relationship between N_w and $D_{0,}$ as observed by Bringi et al. (2003). Also overlaid on this figure are the 5-min-averaged data obtained from analysis of the NASA Joss–Waldvogel disdrometer that were part of the Wallops field experiment. Disdrometer data refer to 3-h measurements and are corrected for the effect known as the disdrometer's dead time (Matrosov et al. 2005). Figure 10 shows that the radar retrievals are reasonable when compared to disdrometer data and emphasizes that, although the retrievals are based on a 2-h radar dataset, the spatial sampling tends to capture a wide range of DSD variability significantly greater than the variability the disdrometer can obtain during the same approximate sampling time.

7. Summary and conclusions

An accurate attenuation correction procedure using the internal self-consistency of radar measurements is used to derive attenuation-corrected polarimetric radar measurements, which in turn are used to retrieve DSD parameters. The full self-consistency solution optimizes for the best estimate of specific and cumulative attenuation as well as specific and cumulative differential attenuation. This technique also produces highly accurate estimates at X band. This paper explores the feasibility of attenuation-corrected measurements for retrieving DSD parameters. Both accurate characterization of raindrop size distribution and the estimation of DSD parameters using remote measurements are needed for inferring rain microphysics useful for regional climatological characterization. However, interpretation of polarimetric radar measurements in rainfall, such as differential reflectivity and specific differential phase

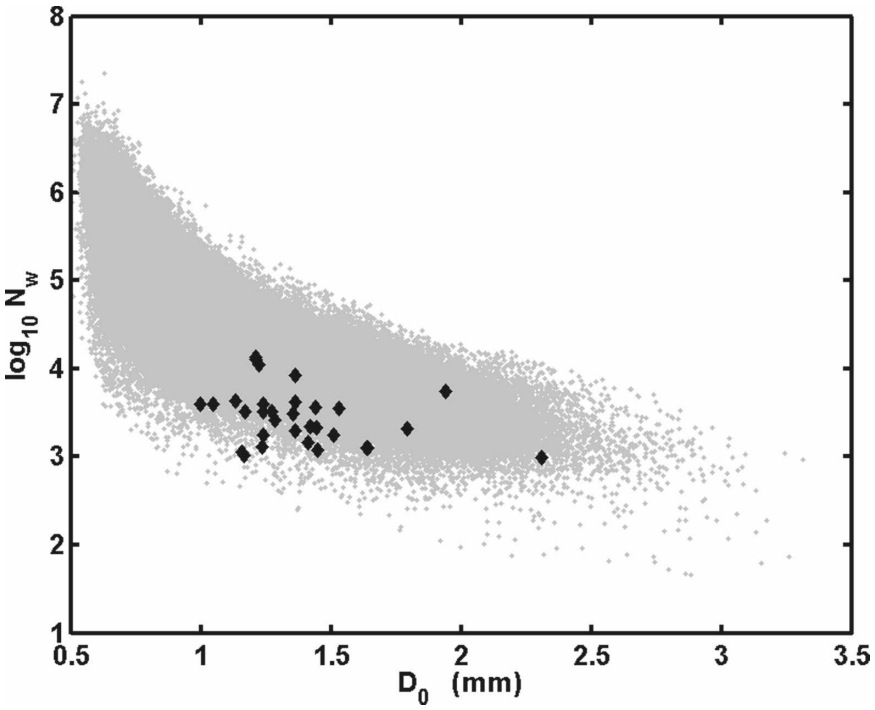

FIG. 10. Scatterplot of $\log_{10} N_w$ vs D_0 (gray dots) as retrieved from the polarimetric radar measurements corresponding to the entire dataset collected on 11 Apr 2001 by the NOAA/ESRL X band. The values refer to about 840 000 values. The black diamonds represent 5-min-averaged DSD measurements obtained by a Joss–Waldvogel disdrometer.

shifts, depends on the mean raindrop shape–size relationship. Following the results obtained on drop shape variability by Gorgucci et al. 2006b, a more robust algorithm is presented to obtain the mean shape of the raindrops from polarimetric radar measurements. When β is known, it is possible to estimate D_0 and N_w from the radar measurements. In this paper, a new set of parameterization for estimating D_0 and N_w at X band is presented.

The retrieval procedure developed in this paper is evaluated by simulation. Parameters of the DSD are obtained from real S-band profiles, which in turn are used to obtain X-band polarimetric radar measurements. Adding their typical measurement errors to X-band profiles and considering the differential phase effect on backscattering, more realistic profiles are obtained and they can give information about the retrieval of DSD parameters. Using this methodology, detailed analysis of the estimated gamma DSD parameters has been performed. The analysis shows a very good performance of D_0 retrieval with very little NSE of 15% and 17% for PB and BC drop shape models, respectively. Similar conclusions are true for $\log_{10} N_w$ retrieval with NSE of 14% and 17%.

Radar measurements collected on 11 April 2001 during the field campaign at the NASA Wallops Island, Virginia, facility by the NOAA/ESRL X-band polarimetric radar are also used in this study as data for comparison.

Using the self-consistency principle of polarimetric measurements in rain, information on drop shape has been obtained and compared with the most widely used drop shape models. From the comparison, it appears that the drops of the studied precipitation event present on average a drop shape that is more oblate than that described by the BZV, ABL, and KCZM models. Moreover, the fact that DSD disdrometer measurements are embedded into the radar DSD retrievals shows that the new microphysical algorithms give reasonable estimations.

Acknowledgments. This research was partially supported by the Italian Ministry of University and Research through the AEROCLOUDS project, by the EU FP6 FLASH project, by the National Science Foundation (ERC-0313747), and the NASA Tropical Rainfall Measuring Mission/Global Precipitation Measurement (TRMM/GPM) programs. Special thanks to Christian Kummerow for providing the NOAA/ESRL X-Pol radar data and to Sergey Matrosov (NOAA–

CIRES) for assistance with decoding the data and for providing the NASA JWD processed data.

REFERENCES

Anagnostou, E. N., M. N. Anagnostou, W. F. Krajewski, A. Kruger, and B. J. Miriovsky, 2004: High-resolution rainfall estimation from X-band polarimetric radar measurements. *J. Hydrometeor.,* **5,** 110–128.

Andsager, K., K. V. Beard, and N. F. Laird, 1999: Laboratory measurements of axis ratios for large raindrops. *J. Atmos. Sci.,* **56,** 2673–2683.

Beard, K. V., and C. Chuang, 1987: A new model for the equilibrium shape of raindrops. *J. Atmos. Sci.,* **44,** 1509–1524.

Brandes, E. A., G. Zhang, and J. Vivekanandan, 2002: Experiments in rainfall estimation with a polarimetric radar in a subtropical environment. *J. Appl. Meteor.,* **41,** 674–685.

——, ——, and ——, 2003: An evaluation of a drop distribution–based polarimetric radar rainfall estimator. *J. Appl. Meteor.,* **42,** 652–660.

Bringi, V. N., and V. Chandrasekar, 2001: *Polarimetric Doppler Weather Radar: Principles and Applications*. Cambridge University Press, 648 pp.

——, ——, N. Balakrishnan, and D. S. Zrnić, 1990: An examination of propagation effects in rainfall at microwave frequencies. *J. Atmos. Oceanic Technol.,* **7,** 829–840.

——, T. D. Keenan, and V. Chandrasekar, 2001: Correcting C-band radar reflectivity and differential reflectivity data for rain attenuation: A self-consistent method with constraints. *IEEE Trans. Geosci. Remote Sens.,* **39,** 1906–1915.

——, V. Chandrasekar, J. Hubbert, E. Gorgucci, W. L. Randeu, and M. Schoenhuber, 2003: Raindrop size distribution in different climatic regimes from disdrometer and dual-polarized radar analysis. *J. Atmos. Sci.,* **60,** 354–365.

Chandrasekar, V., and V. N. Bringi, 1987: Simulation of radar reflectivity and surface measurements of rainfall. *J. Atmos. Oceanic Technol.,* **4,** 464–477.

——, S. Lim, N. Bharadwaj, W. Li, D. McLaughlin, V. N. Bringi, and E. Gorgucci, 2004: Principles of networked weather radar operation at attenuating frequencies. *Proc. Third European Conf. on Radar in Meteorology and Hydrology,* Visby, Sweden, Copernicus GmbH, 109–114.

——, ——, and E. Gorgucci, 2006: Simulation of X-band rainfall observations from S-band radar data. *J. Atmos. Oceanic Technol.,* **23,** 1195–1205.

Gorgucci, E., and L. Baldini, 2007: Attenuation and differential attenuation correction of C-band radar observations using a fully self-consistent methodology. *IEEE Geosci. Remote Sens. Lett.,* **4,** 326–330.

——, G. Scarchilli, and V. Chandrasekar, 1992: Calibration of radars using polarimetric techniques. *IEEE Trans. Geosci. Remote Sens.,* **30,** 853–858.

——, ——, ——, and V. N. Bringi, 2000: Measurement of mean raindrop shape from polarimetric radar observations. *J. Atmos. Sci.,* **57,** 3406–3413.

——, ——, ——, and G. Scarchilli, 2002a: Estimation of raindrop size distribution parameters from polarimetric radar measurements. *J. Atmos. Sci.,* **59,** 2373–2384.

——, L. Baldini, and A. Volpi, 2002b: Polar 55C: An upgraded instrument for polarimetric radar research. Preprints, *Second European Conf. on Radar Meteorology and Hydrology* (*ERAD*), Delft, Netherlands, Copernicus GmbH, 394–399.

——, ——, and V. Chandrasekar, 2006a: What is the shape of raindrops? An answer from radar measurements. *J. Atmos. Sci.,* **63,** 3033–3044.

——, V. Chandrasekar, and L. Baldini, 2006b: Correction of X-band radar observation for propagation effects based on the self-consistency principle. *J. Atmos. Oceanic Technol.,* **23,** 1668–1681.

——, ——, and ——, 2006c: Rainfall estimation from X-band dual polarization radar using reflectivity and differential reflectivity. *Atmos. Res.,* **82,** 164–182.

Hubbert, J., and V. N. Bringi, 1995: An iterative filtering technique for the analysis of copolar differential phase and dual-frequency radar measurements. *J. Atmos. Oceanic Technol.,* **12,** 643–648.

Illingworth, A. J., and T. M. Blackman, 2002: The need to represent raindrop size spectra as normalized gamma distributions for the interpretation of polarization radar observations. *J. Appl. Meteor.,* **41,** 286–297.

——, and R. J. Thompson, 2005: The estimation of moderate rain rates with operational polarisation radar. Preprints, *32nd Conf. on Radar Meteorology,* Albuquerque, NM, Amer. Meteor. Soc., P9R.1.

Keenan, T. D., L. D. Carey, D. S. Zrnić, and P. T. May, 2001: Sensitivity of 5-cm wavelength polarimetric radar variables to raindrop axial ratio and drop size distribution. *J. Appl. Meteor.,* **40,** 526–545.

Martner, B. E., K. A. Clark, S. Y. Matrosov, W. C. Campbell, and J. S. Gibson, 2001: NOAA/ETL's polarization-upgraded X-band "HYDRO" radar. Preprints, *30th Int. Conf. on Radar Meteorology,* Munich, Germany, Amer. Meteor. Soc., 101–103.

Matrosov, S. Y., A. Clark, B. E. Martner, and A. Tokay, 2002: X-band polarimetric radar measurements of rainfall. *J. Appl. Meteor.,* **41,** 941–952.

——, D. E. Kingsmill, B. E. Martner, and F. M. Ralph, 2005: The utility of X-band polarimetric radar for quantitative estimates of rainfall parameters. *J. Hydrometeor.,* **6,** 248–262.

Moisseev, D. N., V. Chandrasekar, C. M. H. Unal, and H. W. J. Russchenberg, 2006: Dual-polarization spectral analysis for retrieval of effective raindrop shapes. *J. Atmos. Oceanic Technol.,* **23,** 1682–1695.

Pruppacher, H. R., and K. V. Beard, 1970: A wind tunnel investigation of the internal circulation and shape of water drops falling at terminal velocity in air. *Quart. J. Roy. Meteor. Soc.,* **96,** 247–256.

Scarchilli, G., E. Gorgucci, V. Chandrasekar, and A. Dobaie, 1996: Self-consistency of polarization diversity measurement of rainfall. *IEEE Trans. Geosci. Remote Sens.,* **34,** 22–26.

Seliga, T. A., and V. N. Bringi, 1976: Potential use of the reflectivity at orthogonal polarizations for measuring precipitation. *J. Appl. Meteor.,* **15,** 69–76.

——, and ——, 1978: Differential reflectivity and differential phase shift: Application in radar meteorology. *Radio Sci.,* **13,** 271–275.

——, ——, and H. H. Al-Khatib, 1981: A preliminary study of comparative measurements of rainfall rate using the differential reflectivity radar technique and a raingauge network. *J. Appl. Meteor.,* **20,** 1362–1368.

Testud, J., E. Le Bouar, E. Obligis, and M. Ali-Mehenni, 2000: The rain profiling algorithm applied to polarimetric weather radar. *J. Atmos. Oceanic Technol.,* **17,** 332–356.

Ulbrich, C., 1983: Natural variations in the analytical form of the raindrop-size distribution. *J. Climate Appl. Meteor.,* **22,** 1764–1775.